# Journal of Materials Chemistry A



**PAPER** 

View Article Online
View Journal | View Issue



Cite this: *J. Mater. Chem. A*, 2019, **7**, 14882

# The effect of local lithium surface chemistry and topography on solid electrolyte interphase composition and dendrite nucleation†

Melissa L. Meyerson,<sup>a</sup> Jonathan K. Sheavly,<sup>b</sup> Andrei Dolocan,<sup>c</sup> Monroe P. Griffin,<sup>a</sup> Anish H. Pandit,<sup>b</sup> Rodrigo Rodriguez,<sup>b</sup> Ryan M. Stephens,<sup>e</sup> David A. Vanden Bout, of Adam Heller, and C. Buddie Mullins abade

With more than 10 times the capacity of the graphite used in current commercial batteries, lithium metal is ideal for a high-capacity battery anode; however, lithium metal electrodes suffer from safety and efficiency problems that prevent their wide industrial adoption. Their intrinsic high reactivity towards most liquid organic electrolytes leads to lithium loss and dendrite growth, which result in poor efficiency and short circuiting. However, the multitude of factors that contribute to dendrite formation make determining a nucleation mechanism extremely difficult. Here, we study the intricate science of dendrite nucleation on metallic lithium by using an array of analytical techniques that provide simultaneous ultra-high spatial sensitivity and chemical selectivity. Our results reveal a 3D picture of the chemical make-up of the native Li surface and the resulting solid electrolyte interphase (SEI) with better than 200 nm resolution. We find that, contrary to the general understanding, the initial surface chemistry, not the topography, is the dominant factor leading to dendrite nucleation. Specifically, inhomogeneously distributed organic material in the native surface leads to inhomogeneously dispersed LiF-rich SEI regions where dendrite nucleation is favored. This has significant implications for battery research as it elucidates a mechanism for inhomogeneous SEI formation, something that is accepted, but not well understood, and highlights the importance of Li surface preparation for experimental studies, which is implicit in battery research, but not directly addressed in the literature. By homogenizing the initial lithium surface composition, and thus the SEI composition, we increase the number of dendrite nucleation sites and thereby decrease the dendrite size, which significantly increases the electrode lifetime.

Received 29th March 2019 Accepted 27th May 2019

DOI: 10.1039/c9ta03371h

rsc.li/materials-a

With the mass popularization of electric vehicles (EVs), alternative energy conversion systems, and portable electronics there is an ever-growing demand for higher energy density batteries to power these new technologies. Advances in battery technology have pushed the practical capacity of graphite anodes in current commercial, rechargeable lithium-ion batteries (LIBs) to their theoretical limits. Thus, it is necessary to replace graphite anodes with a more energy dense material to further increase battery capacity. Lithium metal (3860 mA h g $^{-1}$ ) has more than ten times the capacity of graphite (372 mA h g $^{-1}$ ), making it ideal for a high capacity anode. However,

When Li dendrites deposit on the Li surface they nucleate preferentially in certain locations.<sup>5,6</sup> Many experimental and modeling studies have been conducted to try to elucidate the mechanisms for dendrite formation and growth; however, the causes of dendrite growth are numerous and complex.<sup>7-10</sup> This complexity is reflected in the considerable number of methods

rechargeable Li metal batteries (LMBs) have not yet been commercialized due to major safety and efficiency problems caused by dendrite growth on the Li. When dendrites grow inside a battery, they can short circuit the cell, producing heat and leading to thermal runaway. Additionally, the growth of these high surface area structures consumes both Li and electrolyte as a result of solid electrolyte interphase (SEI) formation. This decreases the coulombic efficiency, and therefore, lifespan, of the battery. <sup>1-3</sup> In practical cells, excess Li and electrolyte is undesirable because it increases the weight and cost of the battery. Therefore, as recently described by Liu *et al.*, it is imperative to understand the relationship between SEI and Li metal in order to develop strategies to enable longer cycle life for high-energy LMBs.<sup>4</sup>

<sup>&</sup>lt;sup>a</sup>Department of Chemistry, University of Texas at Austin, Texas 78712-0231, USA <sup>b</sup>Department of Chemical Engineering, University of Texas at Austin, Texas 78712-0231, USA

Texas Materials Institute, University of Texas at Austin, Texas 78712-0231, USA <sup>a</sup>Center for Electrochemistry, University of Texas at Austin, Texas 78712-0231, USA. E-mail: mullins@che.utexas.edu

<sup>\*</sup>Shell International Exploration & Production Inc., Houston, Texas 77082, USA † Electronic supplementary information (ESI) available. See DOI: 10.1039/c9ta03371h

being researched to suppress dendrite growth and improve battery performance, including the uses of 3D current collectors to confine the Li metal,11 high shear modulus solid or polymer electrolytes to mechanically suppress dendrites, 12,13 artificial SEIs to prevent inhomogeneous reduction of the electrolyte on the Li surface and improve SEI conductivity, 14,15 and electrolyte additives to control the SEI composition.16-19

In early modeling studies, confirmed by experimental work, Chazalviel showed that, at high current densities, the development of a concentration gradient, and subsequent depletion of ions at the electrode surface, leads to dendritic deposition.<sup>7,8</sup> At lower current densities, localized high current density regions develop at sharp edges where the local electric field is enhanced, leading to preferential deposition on these regions. 6,9,10 Although these types of models work well for noble metals, SEI formation due to the high reactivity of Li with nearly all electrolytes complicates the nucleation and growth mechanism of dendrites on Li metal.20

The composition of the SEI that forms as a result of the reaction between metallic Li and organic electrolytes has been extensively studied in numerous different systems and is highly dependent on the type of electrolyte used in the cell as well as electrode chemistry, temperature, and cycling conditions.21 It has been found that the reduction of common carbonate electrolytes and Li salts on the Li surface leads to a wide variety of organic and inorganic compounds, resulting in extremely complex surface chemistry.<sup>22</sup> Despite this complexity, the SEI is generally composed of a denser inorganic layer close to the Li surface with a more porous organic layer in contact with the electrolyte.23 The complexity of the SEI plays a large role in the formation of dendritic structures on Li anodes because Li will preferentially deposit in locations where Li<sup>+</sup> transport is easier, for example in thinner regions of the SEI. As Li continues depositing, it stretches the SEI and can cause it to crack. This crack becomes even more favorable for Li deposition, and a site for dendritic growth.9,24 To further complicate matters, Harry et al. have found yet another factor contributing to dendrite nucleation; the preferential Li deposition on crystalline impurities in the anode surface.25-27

Much of the work already done in the field of Li dendrite nucleation has focused on either the role of the Li surface topography or the role of the overall SEI composition in Li dendrite nucleation and growth, but little work has been done to examine how the local chemistry of the native Li surface affects dendrite nucleation and growth, and local SEI composition. Furthermore, much of the compositional analysis of the native surface and SEI that has been done relies on techniques with relatively low spatial resolution. To our knowledge, no work has yet explored the relationship between surface topography, native surface chemistry, and SEI composition on Li electrodes with an in-plane spatial resolution better than 200 nm, or looked at the effect of the local Li surface chemistry on the SEI chemistry.

In this work, we develop a 3D chemical picture of the native Li surface as well as the SEI that forms as a result of this native surface. By correlating this chemical picture with the surface topography we examine how the surface chemistry and

topography are related and thus determine the dominant factor for dendrite nucleation. Using a combination of atomic force microscopy (AFM) and time-of-flight secondary ion mass spectrometry (ToF-SIMS), we are able to examine the chemistry of the Li surface with much greater spatial resolution than other common techniques such as X-ray photoelectron spectroscopy (XPS) and Fourier-transform infrared spectroscopy (FTIR).21 This allows us to correlate the chemistry of the surface with its topography with better than 200 nm in-plane resolution. We find that on an untreated Li surface there are organic inhomogeneities present before exposure to electrolyte, which lead to the formation of LiF-rich regions in the SEI on these locations. These LiF-rich regions provide preferential locations for Li deposition due to their higher Li-ion conductivity. Comparison of these regions with the surface topography suggests that the chemical composition of the Li surface has a larger impact on preferential dendrite nucleation than topography in this system. This has significant implications for battery research as it elucidates a mechanism for inhomogeneous SEI formation, something that is accepted, but not well understood. It also highlights the importance of Li surface preparation for experimental studies, which is implicit in much battery research, but not directly addressed in the literature.

### **Experimental**

#### Lithium foil treatments

Lithium foil of 99.9% purity and 0.75 mm thickness was purchased from Alfa Aesar (CAS# 7439-93-2). The foil was packaged under argon and stored in an argon-filled glove box with < 0.1 ppm  $O_2$  and  $H_2O$ . The rolled foil was prepared by hand rolling the purchased foil with a polyethylene coated stainless steel rod. The sliced and rolled foil was made by melting a piece of the purchased foil in a stainless steel crucible, removing the floating layer containing the impurities, and pouring the molten lithium into a weigh boat to form an ingot. The ingot was cooled and cut with a craft blade into slices that were about 2 mm thick and then rolled to 0.75 mm with the polyethylene coated rod. ToF-SIMS and AFM were conducted on these samples before exposure to electrolyte and after soaking in 1 M  $LiPF_6$  in 1:1 (v/v) ethylene carbonate (EC):diethyl carbonate (DEC) (dried with molecular sieves to <3 ppm  $H_2O$ ) for 7 hours. The LiPF<sub>6</sub> in EC: DEC electrolyte system was chosen for its commercial relevance, as it is still used more frequently in commercial batteries than the better performing ether electrolytes.

#### Surface analysis

Time-of-flight secondary ion mass spectrometry. ToF-SIMS depth profiles and high-resolution surface maps were obtained with a TOF.SIMS 5 by ION-TOF GmbH, 2010. Lithium samples were transferred from an Ar-filled glovebox to the ToF-SIMS without air exposure by using an interface designed by the Texas Materials Institute of The University of Texas at Austin.<sup>28</sup> The depth profiles were collected in non-interlaced mode alternating the sputtering and analysis beams with all detected

ions having a negative polarity given the electronegative nature of most SEI impurities (carbonates, oxides, fluorinates). A beam of Cs<sup>+</sup> ions (2 keV, ~70 nA measured sample current) impinging upon a 300  $\times$  300  $\mu$ m area was selected for sputtering of the sample surface as this enhances the ionization probability of electronegative species. For analysis, a beam of Bi<sup>+</sup> ions (30 keV,  $\sim$ 3 pA measured sample current) was chosen, raster scanning  $100 \times 100 \ \mu m$  or  $50 \times 50 \ \mu m$  areas, segmented into  $256 \times 256$ pixels and centered within the regressing Cs<sup>+</sup> sputtered areas. The sputtering rate for Li using the Cs<sup>+</sup> beam was calculated at  $\sim$ 1 nm s<sup>-1</sup> based on previous work by Zu et al.<sup>29</sup> The analysis beam was set in either high current mode (HC,  $\sim$ 1  $\mu$ m lateral, that is, in-plane, resolution) or burst alignment mode (BA, that is, high lateral resolution mode, ~200 nm) depending on the required resolution. For example, when the AFM topography had to be correlated with the surface composition the ToF-SIMS maps and depth profiles were acquired in BA mode. The mass resolution in HC mode is 0.001 amu. BA mode has lower mass resolution; however, the m/z peaks for the species analyzed in BA mode were compared to those in HC mode to confirm that there were no other species present in the region covered by the peak in BA mode. The time consuming nature of ToF-SIMS analysis meant only one sample from each treatment process could be analyzed; however, multiple locations on each sample were analyzed and all data shown is representative of these multiple locations, providing reasonable statistics.

Atomic force microscopy. For surface mapping, a Bruker Dimension 3100 AFM that was enclosed in an argon-filled glove box (Innovative Technologies) with <0.1 ppm O<sub>2</sub> and H<sub>2</sub>O was used. All mapping was done in the argon environment to prevent lithium corrosion and to ensure the Bi<sup>+</sup> sputtered spots were protected from any oxygen-related reactions, similar to previous work on an organic photovoltaic system.<sup>30</sup> Topographical images were taken in tapping mode using a Mikro-Masch HQ: NSC15/Al BS silicon probe. The samples were transported both ways between the Ar glove box of the AFM and

the ToF-SIMS high vacuum chamber with an air-free capsule described in the ToF-SIMS section above. Imaging locations were found after transfer by creating a grid around the sample and using the stage x, y coordinates to locate the spots in relation to the grid. Images were plane leveled and the zero point set as the average surface height.

X-ray photoelectron spectroscopy. XPS spectra were obtained with a Kratos Axis Ultra X-ray photoelectron spectrometer, with a monochromatic Al-K $\alpha$  X-ray source ( $h\nu = 1486.5$  eV). Samples were transferred from an Ar filled glovebox using the same transfer capsule as was used for ToF-SIMS. The data were analyzed using CasaXPS software and the peak binding energies were normalized to the adventitious C 1s peak aligned to 284.8 eV. Samples were sputtered with Ar<sup>+</sup> one sample at a time alternating sputtering and analysis with sputtering for 15 s each before analysis for the first three analyses then 30, 60, 120, and 240 s sputtering between subsequent analysis scans. One sample was sputtered at increasing intervals up to 16 min, but no change in signal was detected after 240 s sputtering. At each time point, the area under the peak corresponding to carbonate, oxide, or non-oxygen containing C compounds was normalized to the area under the metallic Li peak and these ratios were compared and correlated with the ToF-SIMS data for the same surface components to create a diagram of the overall surface composition.

#### Electrodeposition and electrochemical testing

Lithium was electrodeposited in a home-built, optical, three-electrode cell described in the ESI, Fig. S1.† The cell was composed of a Li working electrode treated as described above, untreated Li counter and reference electrodes, and 1 M LiPF<sub>6</sub> (BASF) in 1:1 (v/v) ethylene carbonate (99.95%, BASF): diethyl carbonate (99+%, Alfa Aesar) as the electrolyte. A 7.1 mm inner diameter fluorosilicone gasket was used to define the area of the working electrode. The electrolyte, prepared under Ar in a glovebox (<0.1 ppm  $\rm O_2$  and  $\rm H_2O$ ), was dried with EMD Millipore

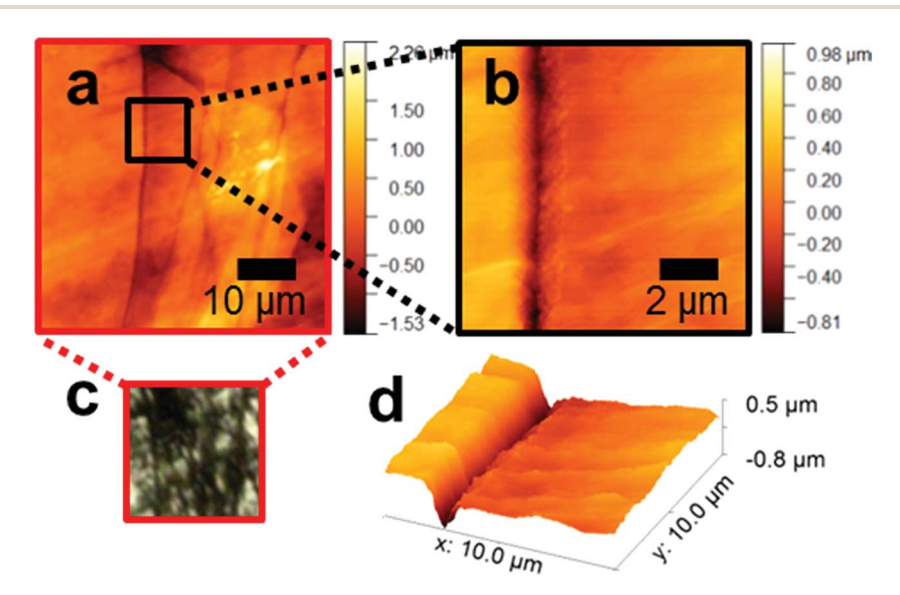


Fig. 1 Atomic force micrographs, (a, b and d), of the vein shown in the optical micrograph in (c), on untreated Li prior to electrolyte exposure.

molecular sieves to less than 3 ppm H<sub>2</sub>O. An Arbin BT 2043 was used to apply a current density of 12.5 or 2.5 mA cm<sup>-2</sup> for 0.5 mA h cm<sup>-2</sup> for the videos taken of the deposition, 1.5 s for the depositions analyzed by ToF-SIMS and AFM, and 60 s for the depositions analyzed by SEM.

For electrochemical testing, 0.75 mm thick Li foil electrodes were prepared under Ar in a glovebox as described under Lithium foil treatments and used in CR2032 coin cells made with a Celgard 2400 polypropylene separator and either a Li counter electrode treated in the same manner or Li<sub>4</sub>Ti<sub>5</sub>O<sub>12</sub> (LTO) electrode. The LTO electrodes were made by slurry casting an 86:7:7 mixture of LTO: Super P conductive carbon: polyvinylidene fluoride (PVDF) in N-methylpyrrolidone (Sigma-Aldrich) onto Cu foil and then calendaring the dried electrodes to  $\sim$ 5  $\mu m$  film thickness. The LTO, Super P, and PVDF were obtained from MTI and the LTO has a median particle size of 1.1 µm and a tap density of 1.5 g cm<sup>-3</sup>. The coin cells were conditioned at C/20 then C/10 then cycled between 1.0 and 2.5 V at a rate of C/5 also using an Arbin BT 2043. A CH Instruments 604D electrochemical analyzer was used for electrochemical impedance spectroscopy (EIS) and galvanostatic linear charge cycling measurements. Electrochemical impedance spectra were taken between 10 mHz and 100 kHz with an amplitude of 5 mV and the galvanostatic linear charge measurements were taken from  $-20 \mu A$  to  $20 \mu A$ .

#### Microscopy

The in situ electrodeposition of Li was recorded with a Firefly DE300 USB Polarizing Dermatoscope and photographs were taken using a Keyence VHX-5000 digital microscope. Scanning electron micrographs of the rolled and sliced and rolled lithium foils, as well as the untreated foil, were obtained before and after lithium deposition with an FEI Quanta 650 scanning electron microscope (SEM). Samples were transferred between the Ar filled glovebox and the SEM using a sealed interface system, Fig. S2, described in the ESI,† to avoid air exposure.

#### Results and discussion

#### Topography of untreated Li

To correlate the initial surface topography of untreated Li with the chemical composition of the surface, we used both atomic force microscopy (AFM) and time-of-flight secondary ion mass

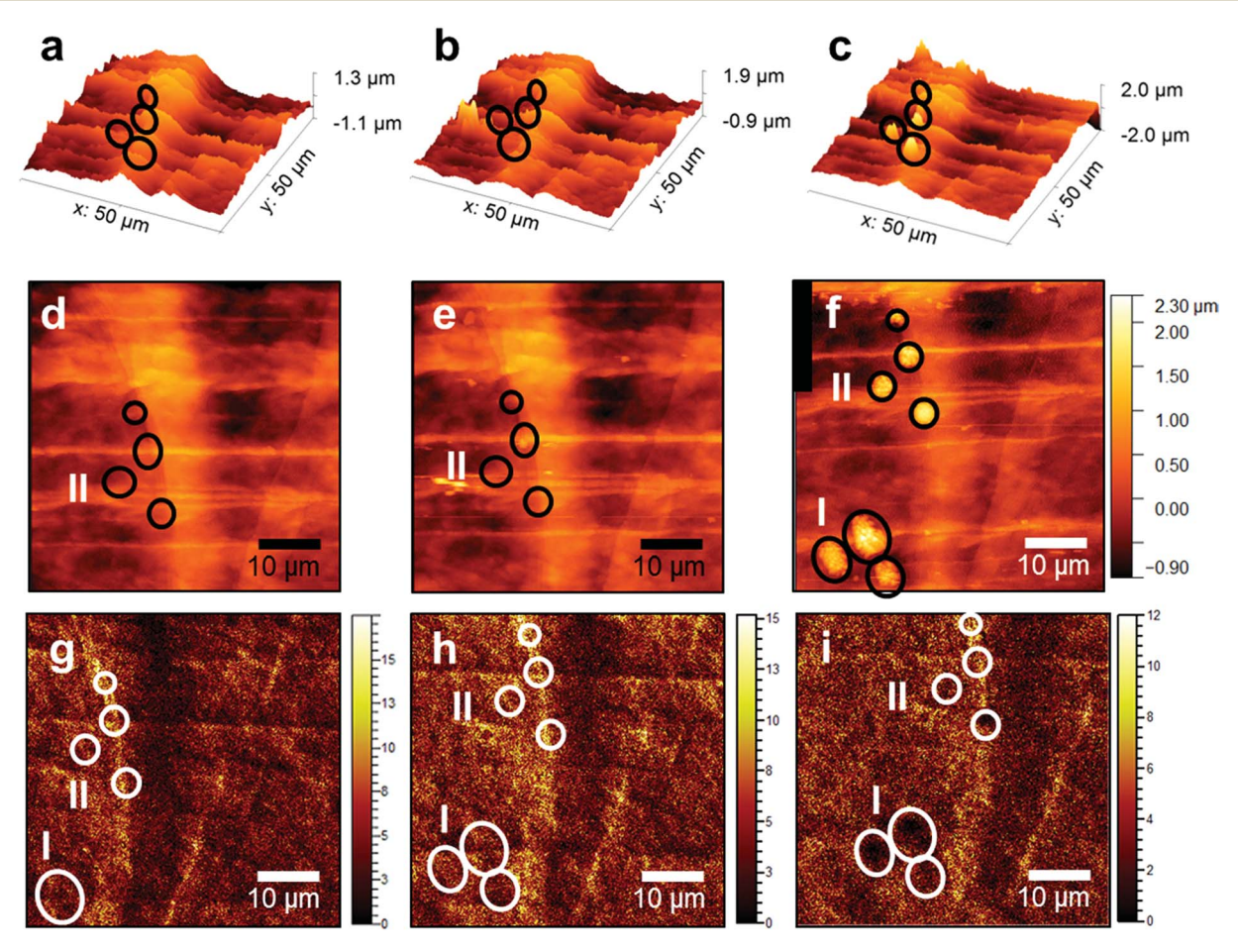


Fig. 2 Atomic force micrographs, (a-f), and ToF-SIMS secondary ion maps (high lateral resolution mode) of  $C_2H^-$ , (g-i), of untreated Li (a, d) and g), are before exposure to electrolyte, (b, e and h), are after soaking in 1 M LiPF<sub>6</sub> in 1:1 EC: DEC for 7 h, and (c, f and i) are after Li electrodeposition at  $12.5 \,\mathrm{mA \, cm^{-2}}$  for  $1.5 \,\mathrm{s}$ . All ion maps are of the top surface layer taken without  $\mathrm{Cs^{+}}$  sputtering and the scale bar corresponds to the number of ion counts.

spectrometry (ToF-SIMS) on the same regions of the sample; AFM for topographical information on the regions and ToF-SIMS for their chemical composition. We analyzed these regions of untreated Li (1) before exposure to electrolyte, (2) after exposure to electrolyte, and (3) after electrodeposition on the surface. In Fig. 1, AFM of the untreated Li surface before exposure to electrolyte shows that lines observed in optical micrographs, Fig. S3,† are ridges and cracks in the surface, which are about 1 µm deep and 0.5–1 µm wide.

There are also ridges, or striations, present on the surface likely arising from the machining process. These striations, along with the cracks/ridges, are visible in optical images taken

There are also ridges, or striations, present on the surface likely arising from the machining process. These striations, along with the cracks/ridges, are visible in optical images taken of the surface, Fig. S3 in the ESI.† To examine the topography of the Li underneath the dendrites, we took AFM scans of the same region of untreated Li before and after electrodepositing Li on the surface. Fig. 2a, d and g correspond to the Li before exposure to electrolyte, Fig. 2b, e and h correspond to the Li after exposure to electrolyte, but before electrodeposition, and Fig. 2c, f and i correspond to the Li after electrodeposition at 12.5 mA cm<sup>-2</sup> for 1.5 s. The circled regions in Fig. 2 correspond to the areas where dendrites are observed on the Li after electrodeposition. Comparing this region before and after exposure to electrolyte for 7 hours shows little change in the size of the cracks or ridges. Comparing the same region before and after Li electrodeposition shows dendrite growth along the ridges and striations. The preferential deposition of Li along these lines is also apparent in scanning electron micrographs taken before and after electrodeposition on the untreated Li surface, Fig. S4.†

From this data it appears that the sharper edges of the ridges and striations lead to preferential dendrite growth. This is in agreement with work by Aurbach's and Tarascon's groups, as well as Li *et al.*, showing that the enhanced electric field at edges leads to preferential Li deposition.<sup>6,9,31</sup>

#### Correlation between topography and chemical composition

In order to explore the relationship between the surface topography described in the previous section and the chemical composition of the surface, we employed ToF-SIMS high resolution mapping, Fig. 2g-i, after each AFM scan. ToF-SIMS mapping before and after exposure to electrolyte shows higher concentrations of C<sub>2</sub>H<sup>-</sup> along the surface of the ridges observed in the AFM maps. Of note, due to the destructive nature of the ToF-SIMS, we were only able to analyze (that is, image) the very top surface and did not sputter deeper into the surface (that is, no depth profiling) of the samples scanned with AFM until after Li deposition; otherwise we would significantly modify the initial Li surface morphology and composition, thereby disturbing the dendrite growth in the sputtered region. Instead, we used ToF-SIMS depth profiling to examine the surface of an untreated sample that had not been exposed to electrolyte and was not electrodeposited on afterward, Fig. 3, to examine the native surface chemistry below the first few nm. Additionally, we sputtered through the dendrites that had deposited on the sample scanned with AFM after Li deposition to examine the chemical composition at the base of the dendrites, Fig. 4.

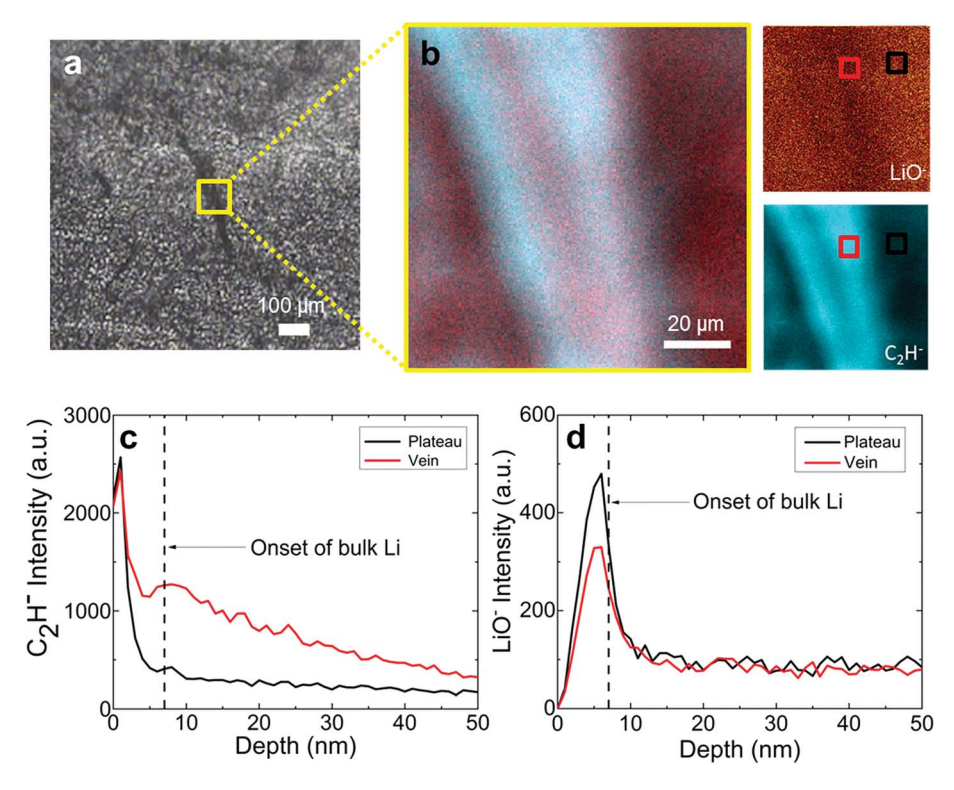


Fig. 3 (a) Optical micrograph of untreated Li foil analyzed by ToF-SIMS, (b) overlay of LiO $^-$  and C $_2$ H $^-$  ToF-SIMS secondary ion maps (high current mode,  $\sim$ 1  $\mu$ m lateral resolution) corresponding to the region highlighted in yellow in (a), and ToF-SIMS depth profiles of (c) C $_2$ H $^-$  and (d) LiO $^-$  on and off the vein of untreated Li.

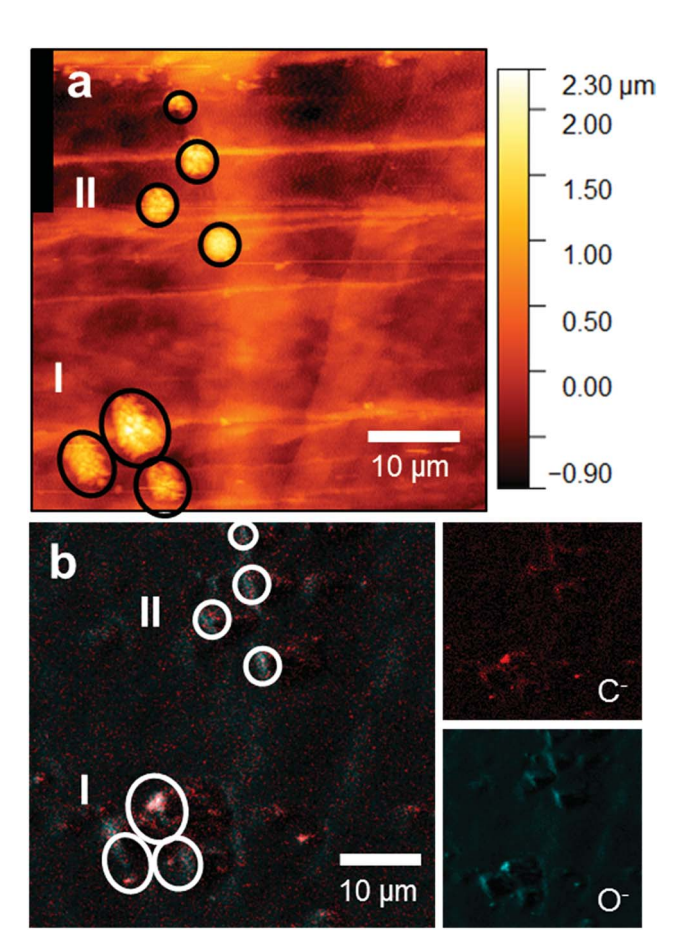


Fig. 4 (a) Atomic force micrograph of untreated Li after Li deposition corresponding to Fig. 2f, (b) 2D rendering of a ToF-SIMS ion map in high lateral resolution mode, overlaying C<sup>-</sup> (red) and O<sup>-</sup> (blue) secondary ion spatial distributions after 9000 s of Cs<sup>+</sup> sputtering. Brighter colors indicate higher counts.

After sputtering through the top few nanometers of an untreated Li sample without exposure to electrolyte, the Li surface still shows that the vein contains a higher concentration of C<sub>2</sub>H<sup>-</sup> than the surrounding area, even extending into the bulk of the Li, Fig. 3. As the surface is sputtered away, the C<sub>2</sub>H<sup>-</sup> localizes into points along the vein, Fig S5.† These individual points appear to provide nucleation sites for dendrites, correlating well with the carbon signal seen at the base of dendrites after sputtering through them, Fig. 4. Here, the onset of bulk Li was determined by the onset of the Li3 - signal and occurs at about 6 nm (based on a sputter rate of  $\sim$ 1 nm s<sup>-1</sup>)<sup>29</sup> both on and off the vein. A diagram of the average composition of the native Li surface as a function of sputter depth can be found in the ESI (Fig. S6†).

In contrast to C<sub>2</sub>H<sup>-</sup>, LiO<sup>-</sup>, indicative of Li<sub>2</sub>O, exists in higher concentrations on the regions surrounding the vein (plateau) than on the vein itself, Fig. 3. Overall, the ToF-SIMS analysis of the untreated Li surface without any exposure to electrolyte shows an inhomogeneous surface chemistry with organic rich veins running through a Li<sub>2</sub>O (and other inorganic species, such as, Li<sub>2</sub>CO<sub>3</sub>, Fig. S7†) rich surface. The preferential Li deposition that we observe, discussed later, correlates with these higher concentrations of organics as well as the topographical ridges observed in the AFM maps.

Combining the results on surface topography from the AFM scans and surface chemistry prior to electrolyte exposure from ToF-SIMS, we find that the optically visible lines on the Li surface are ridges/cracks with about 1 µm height/depth. ToF-SIMS analysis of these ridges shows that they are richer in organic material, but poorer in oxide and other inorganic compounds than the surrounding area. During electrodeposition, Li deposits preferentially along these organic rich ridges, rather than on the oxide rich plateaus. Given that the deposition correlates with both the surface topography and surface

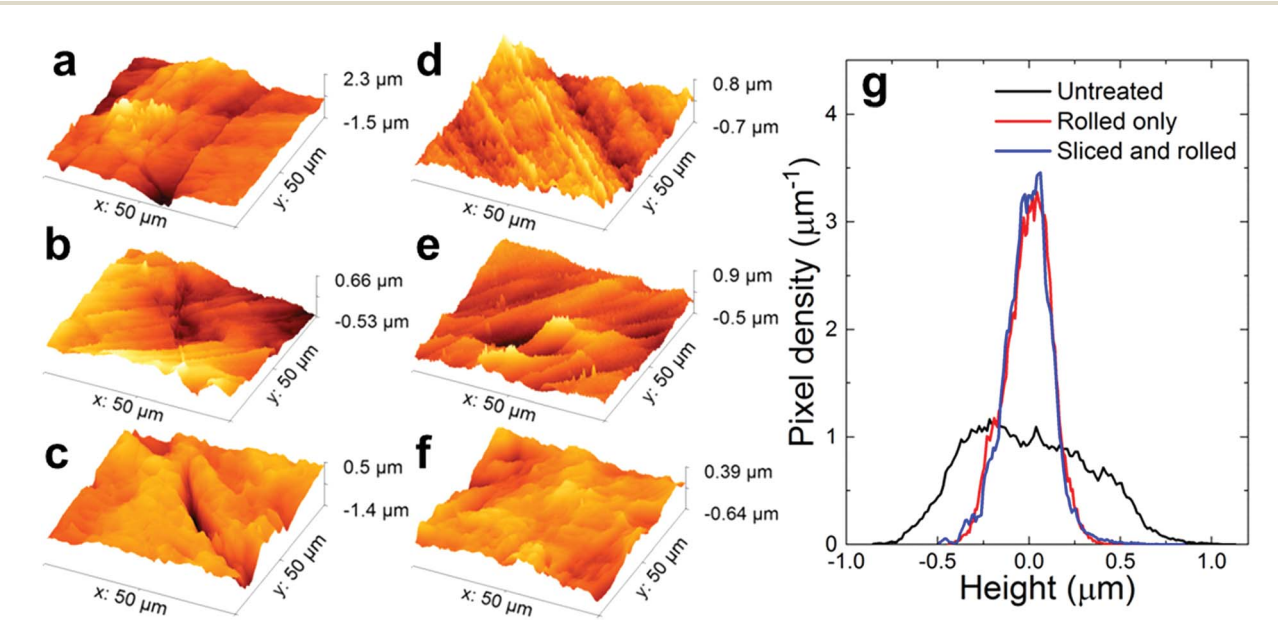


Fig. 5 Atomic force micrographs of (a and d) untreated Li, (b and e) rolled only Li, and (c and f) sliced and rolled Li before exposure to electrolyte. (a-c) Show vein regions while (d-f) show plateau regions. RMS roughness of untreated Li plateau is  $250 \pm 120$  nm, rolled only Li is  $146 \pm 19$  nm, and sliced and rolled Li is  $134 \pm 20$  nm. (g) z-Height histograms of the plateau regions.

chemistry, we cannot conclude that one factor is dominant in the preferential deposition of lithium in this case, so we developed surface treatments to (1) smooth the surface topography and (2) alter the surface composition.

# Surface treatments to remove native surface layer and smooth surface topography

When Li metal is processed in dry air, as it typically is during manufacturing, the highly reactive metal reacts with various environmental constituents to form a passivating film. This passivating film is composed of a thin layer of adventitious carbon on top of a layer of LiOH and Li2CO3, which sits on an oxide rich layer in contact with the metallic Li.32 We confirmed this surface composition on our samples with X-ray photoelectron spectroscopy (XPS) and ToF-SIMS depth profiling, Fig. S6.† To smooth the surface without removing this native oxide layer, we used a polyethylene-coated rod to roll the untreated Li, smoothing out the surface striations present from machining. This treatment is hereafter referred to as "rolled only". To create a smooth surface without the native oxide layer, the untreated Li was melted to form an ingot and then the ingot was sliced inside an argon glovebox with <0.1 ppm H<sub>2</sub>O and <0.1 ppm O<sub>2</sub> to expose a clean face. The cut slice was then rolled with the polyethylene coated rod to yield a similar surface topography to the rolled only Li. This treatment is referred to as "sliced and rolled".

AFM confirms that the surface roughness of both the rolled only and the sliced and rolled surfaces is similar and that both treated surfaces retain the vein features, Fig. 5. Measurements of multiple veins show that they are approximately 1 µm deep (0.9  $\pm$  0.2  $\mu m$  and 1.1  $\pm$  0.4  $\mu m$  for untreated and sliced and rolled Li). The plateau areas of both of the treated surfaces are smoother and more uniform than the untreated Li surface. The average root mean square (RMS) roughness and standard deviation calculated from four separate regions of the rolled only surface and sliced and rolled surface is 146  $\pm$  19 nm and  $134 \pm 20$  nm respectively. In contrast, the untreated Li has an RMS roughness of 250  $\pm$  120 nm indicating it is not only rougher than the treated samples, but also less uniform. Note that RMS measurements were taken only from plateau regions to avoid convolution with roughness from the veins; however, all three surfaces show vein features, Fig. 5a-c. Additionally, the narrowing of the distribution of the surface height on both the vein and plateau regions of the rolled and sliced and rolled surfaces indicates a more uniform surface surrounding the veins, Fig. 5g and S8. The similarity of the distribution of surface heights on the rolled only and sliced and rolled surfaces also corroborates the similarity of these surfaces. The average peak width of the histograms from the plateau region of the untreated Li is 0.7  $\pm$  0.3  $\mu m$  compared to an average peak width of 0.31  $\pm$  0.09  $\mu m$  and 0.25  $\pm$  0.05  $\mu m$  for the rolled only and sliced and rolled surfaces, respectively.

More interesting than the surface topography are the differences in surface chemistry that result from the native surface removal. ToF-SIMS and XPS analyses of the treated surfaces reveal differences in the chemical composition and distribution of the surface layer prior to electrolyte exposure, Fig. 6 and Fig. S6.†

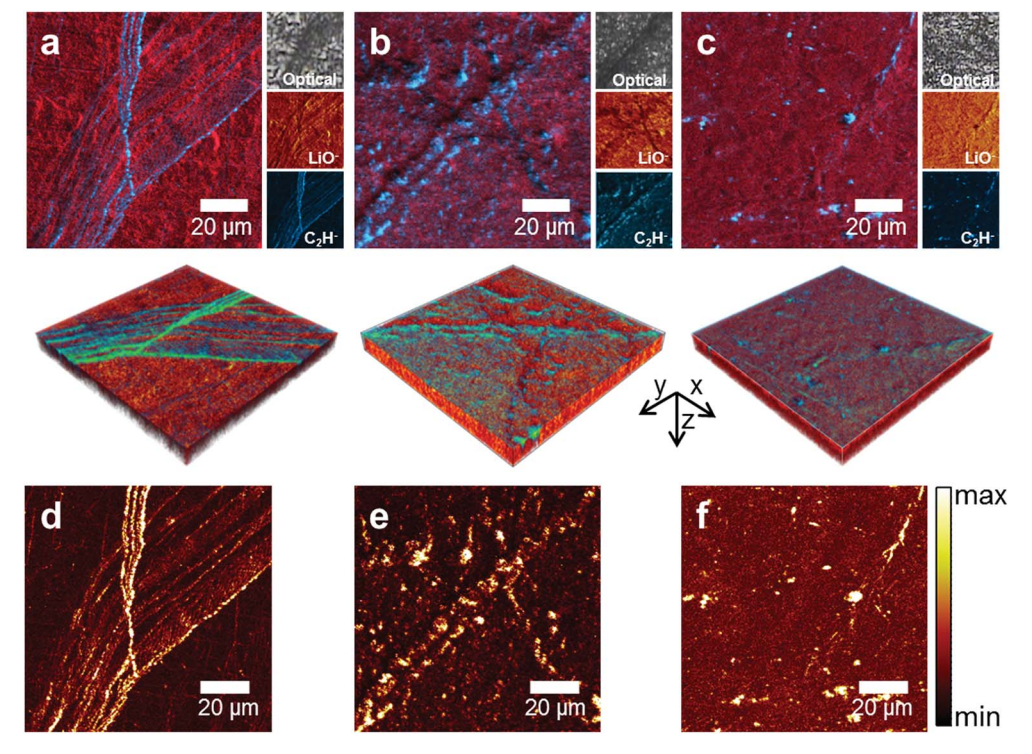


Fig. 6 Top view and 3D rendering of ToF-SIMS depth profiles taken in high lateral resolution mode overlaying secondary ion maps of LiO $^-$  (red), and C<sub>2</sub>H $^-$  (blue-green), from (a) untreated, (b) rolled only, and (c) sliced and rolled Li; and corresponding optical images. (d-f) ToF-SIMS maps showing the C<sub>2</sub>H $^-$  to LiO $^-$  ratio integrating the top 500 nm of the surface.

The native surface on the sliced and rolled Li is an order of magnitude thicker than that on the untreated surface. It also differs compositionally with a higher carbonate to oxide ratio on average, Fig. S9.† However, the most striking differences are in the spatial distribution of oxide and organic material. The organic impurities are more dispersed on the rolled only surface than the untreated surface, but still largely localize along the veins. The organic impurities are even more uniformly spread across the surface of the sliced and rolled Li with no apparent localization in the veins. Given the persistence of veins on all samples and the similarities in surface topography of the rolled only and sliced and rolled surfaces, the differences in deposition patterns on these samples, discussed in the next section, are likely a result of the differences in surface chemical composition rather than topography.

#### Preferential Li electrodeposition on veins

We used an optical three-electrode cell described in the ESI† to observe the in situ electrodeposition of Li on the treated and untreated Li surfaces. We also used a specially built transfer capsule to transfer the electrodes to the SEM without exposing them to air during the transfer, ESI.† Fig. 7 and ESI† Videos show optical time lapse images taken on untreated, rolled only, and sliced and rolled surfaces. As deposition on the untreated Li progresses, the organic-rich ridges, visible as lines in the optical images, darken as a result of dendrite growth on these locations. This preferential deposition along the veins is also apparent at short times for the rolled only surface, although there is also deposition on the plateau areas where the organic material has spread out, as shown in the ToF-SIMS ion map in Fig. 6b. After 100 s, however, the thick dendrite coverage obscures the preferential deposition along the veins on the rolled only Li.

The starkest difference in deposition pattern occurs with the sliced and rolled Li. Although the cracks/ridges are still optically visible on this sample and have similar depth to the untreated sample, the Li does not deposit preferentially along these (no longer organic-rich) regions. Instead it deposits fairly uniformly across the electrode surface following the same pattern as the organic-rich spots. Despite the more uniform deposition on the sliced and rolled surface, it is still dendritic. The trend of increased uniformity on sliced and rolled Li is also seen at a lower current density of 2.5 mA cm<sup>-2</sup>, Fig. S10.† Given the similarities of the surface topographies of the rolled only and sliced and rolled Li surfaces it is unlikely that the differences in electrodeposition on these samples are due to the surface topography. Instead, it appears these differences are due to the distribution of organic material on these surfaces; specifically, the effect of the underlying surface chemistry on the SEI that forms on top of it.

#### Dependence of SEI formation on native surface chemistry

The SEI composition is highly dependent on the chemistry of the Li surface and electrolyte. 33,34 Therefore, the composition of the SEI formed on the inhomogeneous surface of the Li is likely also inhomogeneous, as a result of the carbonate electrolyte reacting differently with Li2O than the organic species formed at the Li foil surface following air exposure, as illustrated in Scheme 1. This could lead to either a thinner or more ionically conductive region in the SEI where the veins are. In order to determine which is the case, we applied a similar ToF-SIMS analysis as that for the native Li surface to examine the composition and thickness of the SEI that formed on the treated and untreated Li samples after soaking in 1 M LiPF<sub>6</sub> in 1:1 (v/v) EC: DEC for 7 hours.

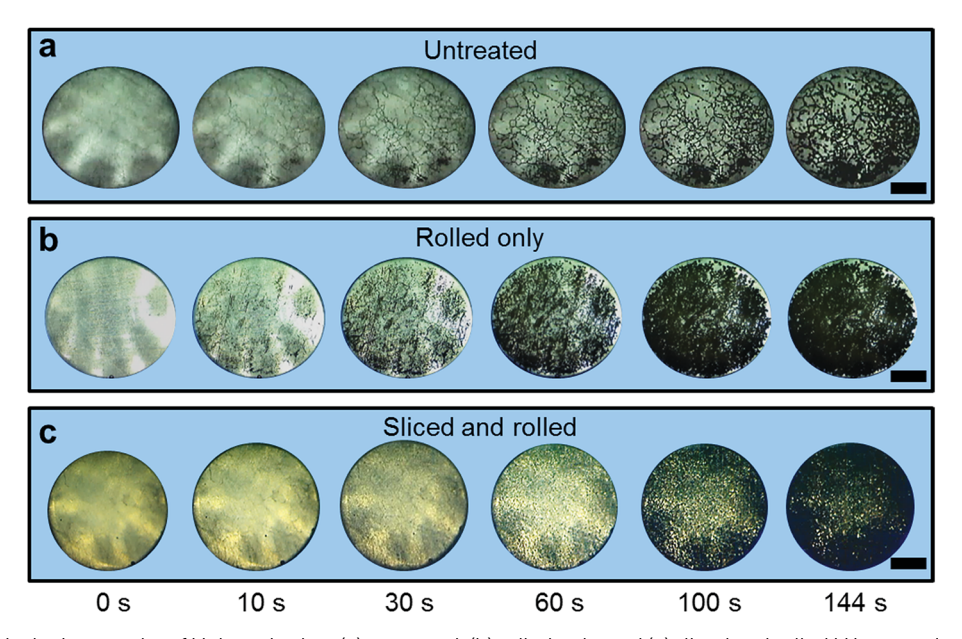
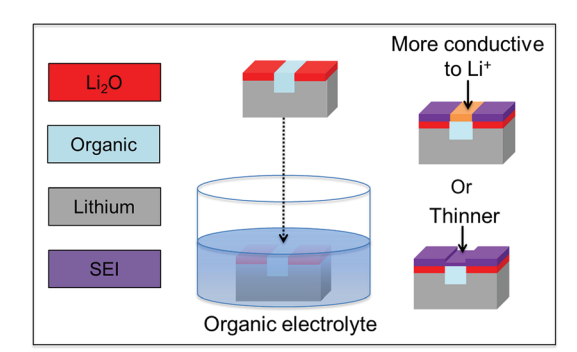


Fig. 7 Time lapse optical micrographs of Li deposited on (a) untreated, (b) rolled only, and (c) sliced and rolled Li in an optical three-electrode cell with 1 M LiPF<sub>6</sub> in 1:1 (v/v) EC: DEC electrolyte. Deposition at 12.5 mA cm<sup>-2</sup>. Scale bar is 2 mm.



**Scheme 1** SEI formation on Li metal surface dependent on underlying surface chemistry.

ToF-SIMS depth profiling on the vein and plateau of untreated Li shows similar SEI thicknesses on both regions, indicated by the appearance of bulk Li at  $\sim$ 6 nm, Fig. 8 and Fig. S11.†

The thicknesses of the common SEI compounds, Li $_2$ O, LiOH, and Li $_2$ CO $_3$ , are also similar on the vein and plateau regions, although there are higher concentrations of these compounds on the plateau than on the vein, Fig. S11.† However, the LiF is higher in concentration on the vein than off and extends much farther into the bulk Li along the vein, which suggests the organic species promote LiF formation. It is well known that LiF

can be formed by the thermal decomposition of  $LiPF_6$  into LiF and  $PF_5$  *via* eqn (1), below. However, LiF can also be produced by the hydrolysis of  $LiPF_6$  or  $PF_5$  with water or alcohols (ROH) such as in eqn (2) and (3):<sup>35,36</sup>

$$LiPF_6 \leftrightarrow LiF + PF_5$$
 (1)

$$LiPF_6 + H_2O \rightarrow LiF + POF_3 + 2HF$$
 (2)

$$PF_5 + ROH \rightarrow POF_3 + HF + RF$$
 (3)

ToF-SIMS secondary ion maps of the untreated Li without exposure to electrolyte indicate higher concentrations of ROH species along the organic-rich vein region than the oxide-rich plateau, Fig. 9a. When untreated Li has been exposed to electrolyte, the vein regions no longer show higher concentrations of ROH species; however, they do show higher concentrations of LiF, POF<sub>3</sub>, and RF, the expected reaction products of eqn (2) and (3), Fig. 9b. The presence of ROH compounds on Li that has not been exposed to electrolyte combined with the disappearance of these compounds and appearance of LiF, POF<sub>3</sub>, and RF on Li that has been exposed to electrolyte suggests that the LiF rich veins are a result of the hydrolysis of LiPF<sub>6</sub> with the ROH containing organic material.

In a study on the role of diffusion and SEI stability on dendrite growth, Ozhabes et al. performed density functional

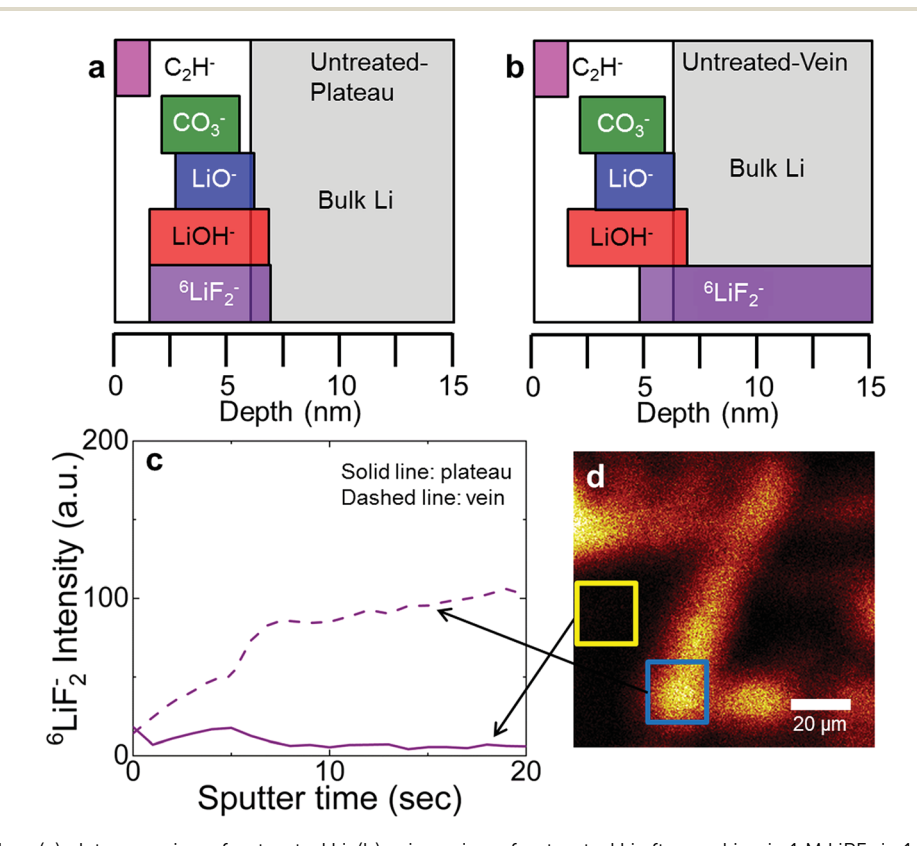


Fig. 8 Diagrams of SEI on (a) plateau region of untreated Li, (b) vein region of untreated Li after soaking in 1 M LiPF<sub>6</sub> in 1:1 EC: DEC for 7 hours. Diagrams constructed from ToF-SIMS depth profiles of the compounds shown in Fig. S11 in the ESI.† (c) Depth profiles of  $^6$ LiF<sub>2</sub> $^-$  on the vein (dashed line) and on the plateau (solid line) corresponding to the regions highlighted in (d). (d) Ion map of  $^6$ LiF<sub>2</sub> $^-$  on untreated Li taken in high current mode.

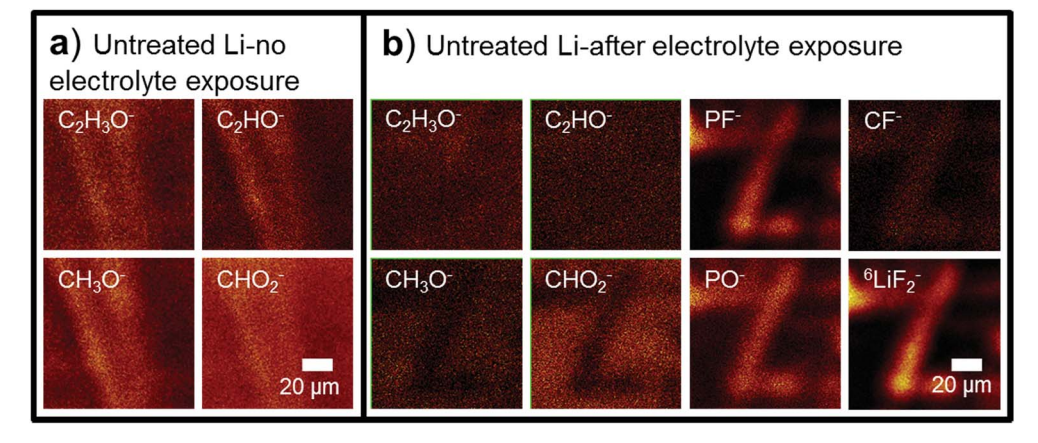


Fig. 9 ToF-SIMS secondary ion maps (high current mode) of alcohol fragments and hydrolysis reaction products on untreated Li (a) without exposure to electrolyte and (b) after soaking in 1 M LiPF<sub>6</sub> in 1:1 EC: DEC for 7 h.

theory calculations comparing the surface energy and diffusion barriers of common SEI components and found that the diffusion barrier of LiF is lower than that of Li<sub>2</sub>O or Li<sub>2</sub>CO<sub>3</sub> for Li<sup>+</sup>.<sup>37</sup> Given that the SEI layer is similar in thickness on the vein and plateau, the lower diffusion barrier of LiF compared to Li2O and Li<sub>2</sub>CO<sub>3</sub> means it should be easier for Li to diffuse into areas that are LiF-rich (vein) compared to areas that are Li<sub>2</sub>O and Li<sub>2</sub>CO<sub>3</sub> rich (plateau). When comparing the surface energies, they found that LiF has a higher surface energy than Li<sub>2</sub>CO<sub>3</sub> due to its small lattice constant and the large electronegativity of F, but that it has a lower surface energy than Li2O.37 Based only on surface energy, it is not clear whether LiF-rich regions would be preferred sites for nucleation over mixed Li<sub>2</sub>CO<sub>3</sub>/Li<sub>2</sub>O-rich regions since it is difficult to say in this case what the true surface energy of each region is. It is also possible that the lower diffusion barrier of LiF is more important than the surface energy, a likely possibility given that Ozhabes et al. have shown a clear correlation between lower diffusion barriers and a longer time to short circuit.<sup>37</sup> This supports the theory that the underlying organic material promotes the growth of a more Li<sup>+</sup> conductive SEI.

ToF-SIMS depth profiling also shows that the differences in the SEI composition of the untreated compared to the treated Li surfaces after soaking in electrolyte for 7 hours depend on the underlying chemistry. The SEI on the sliced and rolled Li is more homogeneous than that on the untreated Li, as expected based on the underlying surface composition, Fig. 10. The thickness of the SEI on the treated surfaces follows same trend as the respective thicknesses of the native layer, with slightly thicker SEI (~7 nm) on rolled only Li than untreated Li (~6 nm) and the thickest SEI on sliced and rolled Li (~13 nm), Fig. S12.† Diagrams of the native surface composition and SEI composition on rolled only and sliced and rolled electrodes are shown in Fig. S12.† The SEI compounds, including LiF, are more uniformly dispersed on the rolled only Li surface than the untreated surface, corresponding to similar changes in the native surface layer. Further, the sliced and rolled Li has the most uniform SEI corresponding to the most uniform (that is, most chemically homogeneous) native surface layer, Fig. 10.

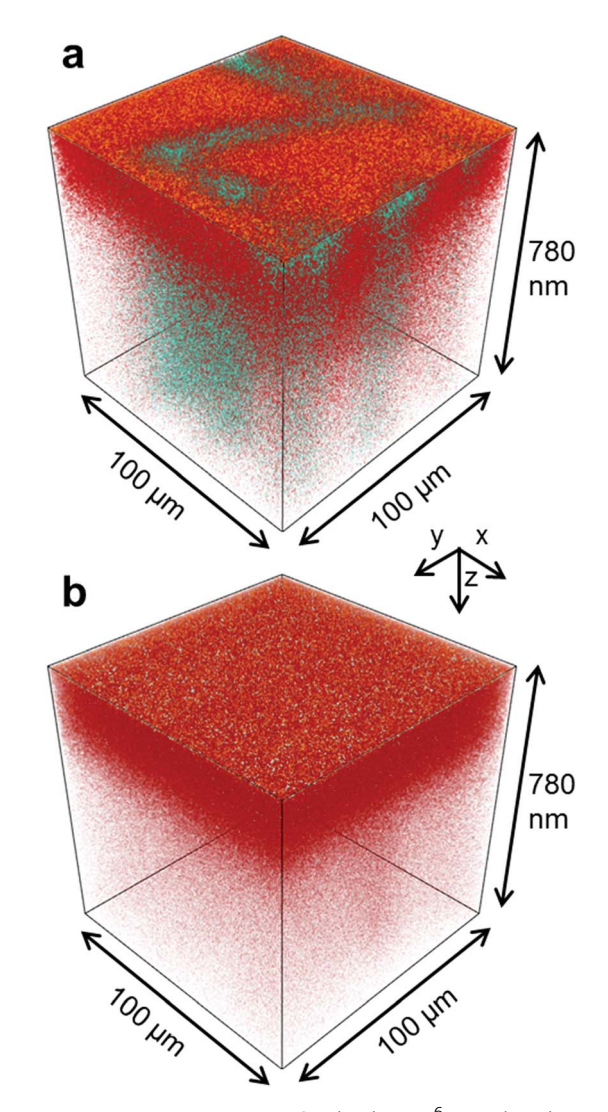


Fig. 10 3D reconstruction of LiO<sup>-</sup> (red) and <sup>6</sup>LiF<sub>2</sub><sup>-</sup> (blue) from (a) untreated Li, and (b) sliced and rolled Li after soaking in 1 M LiPF<sub>6</sub> in 1:1 EC : DEC for 7 hours. 100  $\times$  100  $\mu m$  area, 780 nm depth.

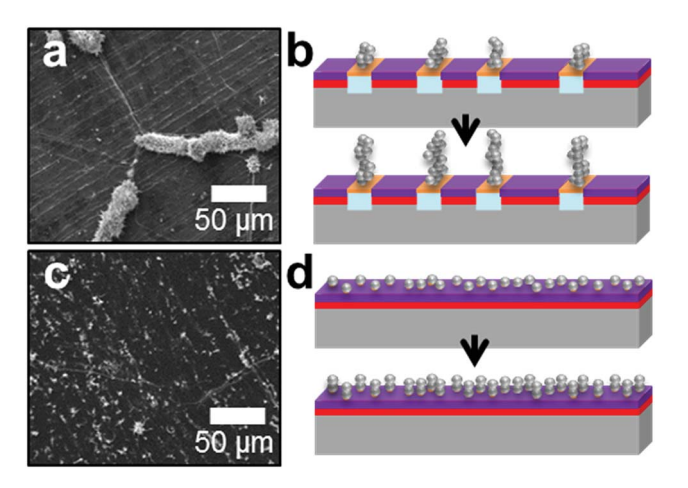


Fig. 11 Scanning electron micrographs of Li deposited on (a) untreated Li, and (c) sliced and rolled Li for 20 s and diagrams of deposition of the same amount of Li on untreated Li with large, segregated impurities (b), and small, homogeneous impurities (d).

Although thicker, the SEI on the sliced and rolled electrode is more conductive to Li<sup>+</sup> than the SEI on the untreated electrode. This is confirmed by electrochemical impedance spectroscopy of Li/Li symmetric cells exposed to 1 M LiPF<sub>6</sub> in 1:1 (v/v) EC: DEC for 7 hours, where the SEI resistance of the untreated Li was calculated to be  $24~\Omega$  nm<sup>-1</sup> compared to  $11~\Omega$  nm<sup>-1</sup> for the sliced and rolled electrode. However, the exchange current densities of both untreated and sliced and rolled surfaces were similar,  $i_0 = 0.16~\mathrm{mA~cm^{-2}}$ , indicating that the kinetics of lithium reduction are similar in both SEIs. This value was determined using galvanostatic linear charge cycling from

 $-20~\mu A$  to 20  $\mu A$  and fitting the resulting potential to the approximation of the Butler-Volmer equation at low overpotentials,  $i=-i_0f\eta$ , where i is the current, f=F/RT (F is Faraday's constant, R is the ideal gas constant, and T is the temperature in Kelvin), and  $\eta$  is the overpotential.<sup>38</sup>

Considering both the topographical and chemical differences in the Li surface, the underlying surface chemistry appears to influence the SEI chemistry more than the surface topography does. These differences in the SEI chemistry are most likely the cause of the preferential deposition of Li through the LiF-rich areas, given the ease of Li diffusion in these regions.

#### Practical implications of surface homogeneity

SEM of the treated and untreated surfaces after electrodeposition at 12.5 mA cm<sup>-2</sup>, Fig. 11 and S13,† show smaller dendrites that are more dispersed on the sliced and rolled surface than on the untreated Li surface. The dispersion of the organic material on the sliced and rolled surface creates a larger number of LiFrich nucleation sites on this surface than on the untreated Li that has localized organic impurities. After initial Li clusters have formed on nucleation sites it is more energetically favorable for Li to deposit on existing clusters than it is for Li to deposit on new sites.<sup>39,40</sup> Thus, it makes sense that a surface with a greater number of nucleation sites would have smaller dendrites, as the same number of Li<sup>+</sup> ions is distributed to a greater number of sites; therefore, the structures that grow are smaller, as there is less Li going to each site, Fig. 11.

This also makes sense from the perspective of surface energy if the increased homogeneity of the sliced and rolled surface leads to a smaller variation in surface energies across the

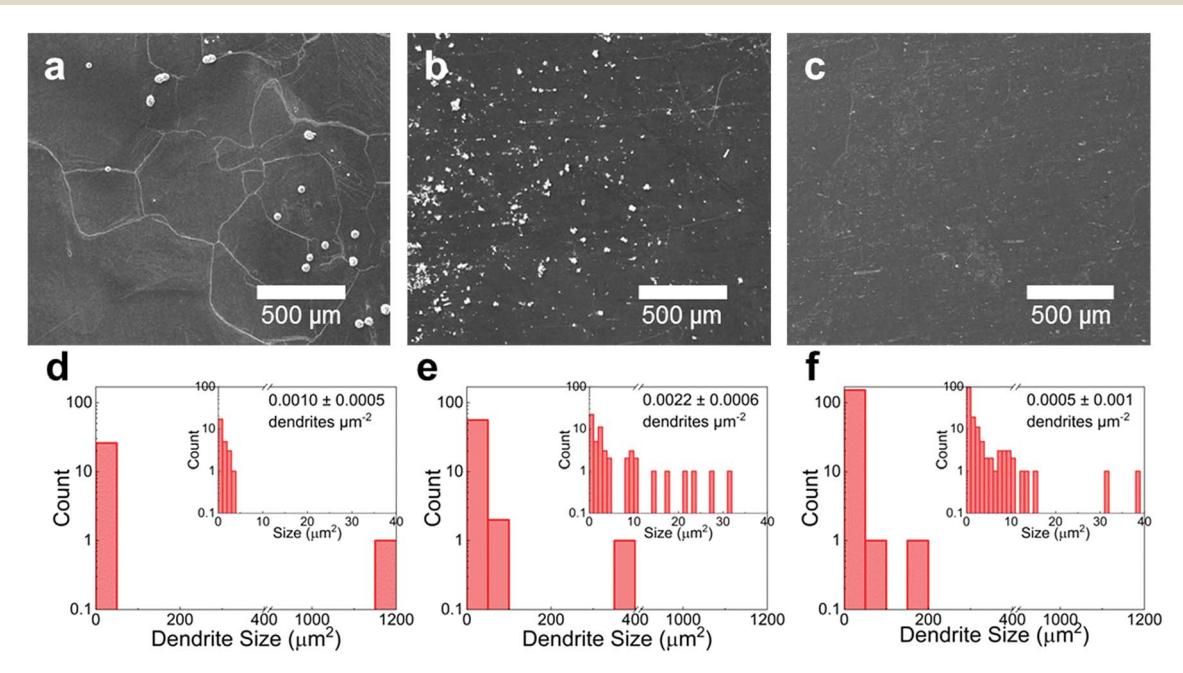


Fig. 12 Scanning electron micrographs of lithium electrodeposited on (a) untreated, (b) rolled only, and (c) sliced and rolled lithium at 2.5 mA cm $^{-2}$  for 60 s, histograms of dendrite sizes from scanning electron micrographs (d) untreated, (e) rolled only, and (f) sliced and rolled Li. Dendrite count comes from  $\sim$ 27 000  $\mu$ m $^2$ . Bin size in main graphs and insets is 50  $\mu$ m $^2$  and 1  $\mu$ m $^2$  respectively.

electrode. When the variation in surface energies is smaller there is a corresponding decrease in the variation of dendrite sizes, as seen in the smaller spread of dendrite sizes on the sliced and rolled electrode compared to the untreated electrode. The differences in nucleation density may also be related to surface energy in this system. The interfacial energy is directly proportional to the critical radius of a nucleus, and the radius of the nucleus is directly proportional to the radius of the screening zone around that nucleus. In the case of the untreated Li surface, a larger critical radius would lead to a larger screening zone around the dendrite nucleation site, causing dendrites to be less densely distributed across the surface than they are on the treated electrodes.

To quantify these differences we electrodeposited Li at 2.5 mA cm $^{-2}$  for 60 s, so that we could distinguish individual nucleation sites before the dendritic clusters had grown together. Scanning electron micrographs, Fig. 12, of the untreated surface show the largest dendrites with most of the Li deposited going to dendrites above 1000  $\mu m^2$  and a nucleation density of 0.0010  $\pm$  0.0005 dendrites per  $\mu m^2$ . Dendrites on rolled only Li are smaller, with the largest dendrites less than 400  $\mu m^2$ , and have a higher nucleation density, 0.0022  $\pm$  0.0006 dendrites per  $\mu m^2$ . Dendrites on the sliced and rolled Li are the smallest and most densely distributed with the largest dendrites less than 200  $\mu m^2$  and a nucleation density of 0.005  $\pm$  0.001 dendrites per  $\mu m^2$ .

This difference in dendrite size and nucleation density leads to improved performance for coin cells with sliced and rolled Li electrodes compared to coin cells with untreated Li electrodes run at a C-rate of 0.2C, such that Li transport is not limited, Fig. 13. The faster capacity fade for the untreated cells can be attributed to the increased build-up of dead Li on the untreated surface compared to the sliced and rolled surface. The stripping of Li from the base of dendrites causes the upper portion of the dendrite to become electrically disconnected from the electrode, leaving behind dead Li.<sup>24,44</sup> Smaller dendrites that are in closer contact with the Li surface mean less of the deposited Li is lost as the upper portions of the dendrites lose contact with

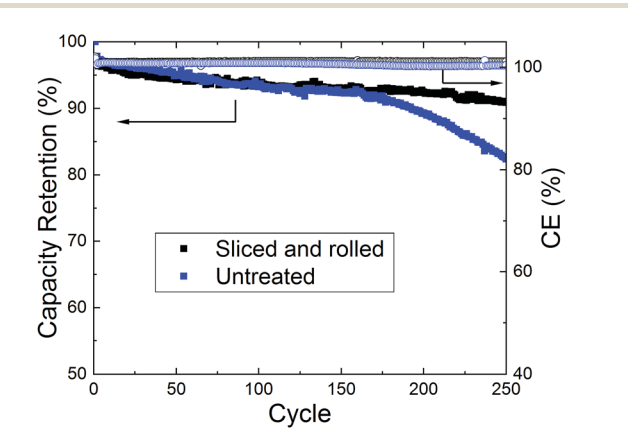


Fig. 13 Capacity retention for untreated Li vs.  $\text{Li}_4\text{Ti}_5\text{O}_{12}$  (LTO) and sliced and rolled Li vs. LTO coin cells cycled at C/5. Note: data shown from single coin cell is representative of performance of multiple cells tested.

the current collector during cycling. Consequently, more dead Li builds up on the untreated Li surface during Li stripping given that more Li is left behind in the upper portions of the larger dendrites on this surface.

#### Conclusions

By employing both ToF-SIMS high resolution mapping and depth profiling, as well as AFM imaging, the native Li surface chemistry was examined with a high level of detail and correlated with the surface topography, solid electrolyte interphase (SEI) chemical composition, and localization of Li electrodeposition, creating a 3D chemical and physical picture of the Li surface before and after exposure to electrolyte. Prior to electrolyte exposure, the native Li surface of untreated Li metal contains localized, micron-sized veins of organic material that correspond with topographical ridges/cracks; these organic-rich regions provide preferential sites for Li electrodeposition. After electrolyte exposure, these organic-rich areas grow an SEI that is of the same thickness as the surrounding areas, but richer in LiF, likely due to the hydrolysis of LiPF<sub>6</sub> with alcohols found in higher concentrations in those regions compared with that of the surrounding plateaus, resulting in locations that are more conductive to Li<sup>+</sup>, and thus leading to preferential Li deposition.

Li metal that has been rolled with a polyethylene-coated rod to homogenize the surface topography is smoother than the untreated Li, but still contains ridges/cracks. When the native surface of the Li is not removed to homogenize the composition, dendrites still grow preferentially along the organic-rich veins, which likewise remain. However, when the native surface is removed, homogenizing the Li surface composition, and thus the SEI, dendrite growth is no longer localized to the ridges/cracks, but instead spreads out across the entire surface. When Li<sup>+</sup> transport is not limited by concentration polarization, the increase in number of nucleation sites on the sliced and rolled Li surface results in smaller dendrites, which extends the cycling life of Li coin cells by reducing the amount of dead Li formed during each cycle.

These results suggest that although both surface topography and surface chemistry play a role in the preferential nucleation of Li dendrites, it is the initial inhomogeneous surface composition leading to inhomogeneous SEI composition that is the dominant factor for dendrite nucleation at or below 0.2C cycling rate. This not only elucidates a mechanism for inhomogeneous SEI formation, but also highlights the importance of considering the native Li surface when designing improved Li surface coatings in order to make Li metal anodes a reality for commercial batteries.

#### Conflicts of interest

There are no conflicts to declare.

## Acknowledgements

Financial support for this research was provided by Shell and the Robert A. Welch Foundation (CBM F-1436, AH F-1131). NSF grant CBET-1603491 partially supported M. Meyerson during some of this project. The authors thank K. Ravi-Chandar for the use of his Keyence VHX-5000 digital microscope, H. Celio for discussions about the XPS, and the Texas Materials Institute, K. Ohlinger, and S. McDonald for the design of the SEM vacuum transfer module.

#### References

- 1 W. Xu, J. Wang, F. Ding, X. Chen, E. Nasybulin, Y. Zhang and J.-G. Zhang, *Energy Environ. Sci.*, 2014, 7, 513–537.
- 2 X.-B. Cheng, R. Zhang, C.-Z. Zhao and Q. Zhang, *Chem. Rev.*, 2017, 117, 10403–10473.
- 3 N.-S. Choi, Z. Chen, S. A. Freunberger, X. Ji, Y.-K. Sun, K. Amine, G. Yushin, L. F. Nazar, J. Cho and P. G. Bruce, *Angew. Chem., Int. Ed.*, 2012, **51**, 9994–10024.
- 4 J. Liu, Z. Bao, Y. Cui, E. J. Dufek, J. B. Goodenough, P. Khalifah, Q. Li, B. Y. Liaw, P. Liu, A. Manthiram, Y. S. Meng, V. R. Subramanian, M. F. Toney, V. V. Viswanathan, M. S. Whittingham, J. Xiao, W. Xu, J. Yang, X.-Q. Yang and J.-G. Zhang, *Nat. Energy*, 2019, 4, 180–186.
- 5 D. Aurbach, Y. Gofer and J. Langzam, J. Electrochem. Soc., 1989, 136, 3198–3205.
- 6 L. Gireaud, S. Grugeon, S. Laruelle, B. Yrieix and J.-M. Tarascon, *Electrochem. Commun.*, 2006, 8, 1639–1649.
- 7 C. Brissot, M. Rosso, J.-N. Chazalviel and S. Lascaud, *J. Power Sources*, 1999, **81**, 925–929.
- 8 J.-N. Chazalviel, *Phys. Rev. A: At., Mol., Opt. Phys.*, 1990, 42, 7355.
- 9 Y. S. Cohen, Y. Cohen and D. Aurbach, J. Phys. Chem. B, 2000, 104, 12282–12291.
- 10 G. Bieker, M. Winter and P. Bieker, *Phys. Chem. Chem. Phys.*, 2015, **17**, 8670–8679.
- 11 W. Go, M.-H. Kim, J. Park, C. H. Lim, S. H. Joo, Y. Kim and H.-W. Lee, *Nano Lett.*, 2019, **19**, 1504–1511.
- 12 A. Mauger, M. Armand, C. M. Julien and K. Zaghib, *J. Power Sources*, 2017, **353**, 333–342.
- 13 Z. Zhang, Y. Shao, B. Lotsch, Y.-S. Hu, H. Li, J. Janek, L. F. Nazar, C.-W. Nan, J. Maier, M. Armand and L. Chen, Energy Environ. Sci., 2018, 11, 1945–1976.
- 14 G. A. Umeda, E. Menke, M. Richard, K. L. Stamm, F. Wudl and B. Dunn, *J. Mater. Chem.*, 2011, 21, 1593–1599.
- 15 F. Marchioni, K. Star, E. Menke, T. Buffeteau, L. Servant, B. Dunn and F. Wudl, *Langmuir*, 2007, 23, 11597–11602.
- 16 S. M. Wood, C. H. Pham, R. Rodriguez, S. S. Nathan, A. D. Dolocan, H. Celio, J. P. de Souza, K. C. Klavetter, A. Heller and C. B. Mullins, ACS Energy Lett., 2016, 1, 414–419.
- 17 H. Ota, K. Shima, M. Ue and J. Yamaki, *Electrochim. Acta*, 2004, **49**, 565–572.
- 18 S. Shiraishi, K. Kanamura and Z. Takehara, *J. Electrochem. Soc.*, 1999, **146**, 1633–1639.
- 19 J. C. Burns, N. N. Sinha, G. Jain, H. Ye, C. M. VanElzen, E. Scott, A. Xiao, W. M. Lamanna and J. R. Dahn, J. Electrochem. Soc., 2013, 160, A2281–A2287.

- 20 D. Aurbach, B. D. McCloskey, L. F. Nazar and P. G. Bruce, Nat. Energy, 2016, 1, 16128.
- 21 P. Verma, P. Maire and P. Novák, *Electrochim. Acta*, 2010, 55, 6332–6341.
- 22 D. Aurbach, E. Zinigrad, Y. Cohen and H. Teller, *Solid State Ionics*, 2002, **148**, 405–416.
- 23 D. Aurbach, J. Power Sources, 2000, 89, 206-218.
- 24 J. Yamaki, S. Tobishima, K. Hayashi, K. Saito, Y. Nemoto and M. Arakawa, J. Power Sources, 1998, 74, 219–227.
- 25 K. J. Harry, D. T. Hallinan, D. Y. Parkinson, A. A. MacDowell and N. P. Balsara, *Nat. Mater.*, 2013, 13, 69–73.
- 26 K. J. Harry, X. Liao, D. Y. Parkinson, A. M. Minor and N. P. Balsara, J. Electrochem. Soc., 2015, 162, A2699–A2706.
- 27 N. S. Schauser, K. J. Harry, D. Y. Parkinson, H. Watanabe and N. P. Balsara, J. Electrochem. Soc., 2015, 162, A398–A405.
- 28 H. Celio, US Pat. Application, 20150037904, 2015.
- 29 C. Zu, A. Dolocan, P. Xiao, S. Stauffer, G. Henkelman and A. Manthiram, *Adv. Energy Mater.*, 2016, **6**, 1501933.
- 30 M. P. Griffin, R. Gearba, K. J. Stevenson, D. A. Vanden Bout and A. Dolocan, *J. Phys. Chem. Lett.*, 2017, **8**, 2764–2773.
- 31 Q. Li, B. Quan, W. Li, J. Lu, J. Zheng, X. Yu, J. Li and H. Li, *Nano Energy*, 2018, **45**, 463–470.
- 32 I. Ismail, A. Noda, A. Nishimoto and M. Watanabe, *Electrochim. Acta*, 2001, **46**, 1595–1603.
- 33 E. Peled, J. Electrochem. Soc., 1979, 126, 2047.
- 34 X.-B. Cheng, R. Zhang, C.-Z. Zhao, F. Wei, J.-G. Zhang and Q. Zhang, *Adv. Sci.*, 2016, 3, 1500213.
- 35 K. Tasaki, K. Kanda, S. Nakamura and M. Ue, *J. Electrochem. Soc.*, 2003, **150**, A1628.
- 36 A. Guéguen, D. Streich, M. He, M. Mendez, F. F. Chesneau, P. Novák and E. J. Berg, *J. Electrochem. Soc.*, 2016, 163, A1095–A1100.
- 37 Y. Ozhabes, D. Gunceler and T. A. Arias, 2015, ArXiv150405799 Cond-Mat Physicsphysics.
- 38 A. J. Bard and L. R. Faulkner, *Electrochemical methods: Fundamentals and applications*, John Wiley & Sons, Inc., 2nd edn, 2001.
- 39 F. Sagane, K. Ikeda, K. Okita, H. Sano, H. Sakaebe and Y. Iriyama, *J. Power Sources*, 2013, 233, 34–42.
- 40 A. Pei, G. Zheng, F. Shi, Y. Li and Y. Cui, *Nano Lett.*, 2017, **17**, 1132–1139.
- 41 R. L. Deutscher and S. Fletcher, *J. Electroanal. Chem. Interfacial Electrochem.*, 1990, 277, 1–18.
- 42 D. R. Ely and R. E. García, *J. Electrochem. Soc.*, 2013, **160**, A662–A668.
- 43 K. I. Popov, S. S. Djokic and B. N. Grgur, Fundamental Aspects of Electrometallurgy, Kluwer Academic/Plenum Publishers, New York, 2002.
- 44 J.-H. Cheng, A. A. Assegie, C.-J. Huang, M.-H. Lin, A. M. Tripathi, C.-C. Wang, M.-T. Tang, Y.-F. Song, W.-N. Su and B. J. Hwang, *J. Phys. Chem. C*, 2017, 121, 7761–7766.